



UNIVERSITEIT VAN AMSTERDAM

MSc Physics and Astronomy

Track: Advanced Matter and Energy Physics

Master Thesis

---

# Resonant metagratings for spectral and angular control of light in photovoltaics

---

*by Floris Charlie Uleman*

*11740418*

July 22, 2019

60 ECTS

September 2018 - July 2019

Supervisor:

*Prof. dr. A. (Albert) Polman*

Second examiner:

*Dr. K. (Katerina) Newell*





# Resonant metagratings for spectral and angular control of light in photovoltaics

Floris Uleman

## Abstract

We design a semi-transparent metasurface that enables wavefront shaping on resonance in reflection. Supercells of metagratings can be combined in arrays to shape any desired wide-angle scattering pattern at a specific wavelength range. The spectral response in reflection is controlled by manipulating the shape of silicon Mie-like resonators that exhibit resonant scattering profiles. The directivity and power towards different diffraction orders is controlled by adjusting the pitch, the position and shape of the individual gratings. We experimentally demonstrate metasurfaces composed of silicon nanowires on a sapphire substrate that create a Lambertian scattering profile at  $\lambda = 650$  nm. The scattering efficiency of the silicon nanowires is enhanced at resonance. Furthermore, the transmission of the supercell is tailored such that the external quantum efficiency is 80 – 90% over a broad angular range. These geometries can find application in light trapping layers for thin film solar cells, efficient colorful photovoltaics as well as spectral splitting layers for perovskite-silicon tandem devices.



---

# Contents

---

<b>1</b>	<b>Introduction</b>	<b>1</b>
<b>2</b>	<b>Theory: spectral and angular control of light</b>	<b>5</b>
2.1	Mie-like resonances . . . . .	5
2.2	Diffraction grating . . . . .	7
2.3	Lambertian scattering . . . . .	9
<b>3</b>	<b>Optimization and design</b>	<b>11</b>
3.1	Time-domain modeling by FDTD . . . . .	11
3.1.1	Setup and analysis . . . . .	11
3.2	Large angle scattering . . . . .	13
3.2.1	Single particle in periodic boundary conditions . . . . .	13
3.2.2	Designing the unit cell . . . . .	14
3.2.3	Spectral response of the unit cell . . . . .	15
3.2.4	Angular response of the unit cell . . . . .	17
<b>4</b>	<b>Fabrication</b>	<b>19</b>
4.1	Fabrication steps of the supercell . . . . .	19
4.2	SEM images of the fabricated supercell . . . . .	21
<b>5</b>	<b>Optical measurements of large angle scattering</b>	<b>23</b>
5.1	Spectral response: integrating sphere . . . . .	23
5.1.1	First and zeroth order reflection . . . . .	24
5.2	Angular response: rotating stage . . . . .	26
5.2.1	Reflection to every angle . . . . .	26
5.3	External quantum efficiency . . . . .	28
<b>6</b>	<b>Conclusion and outlook</b>	<b>31</b>
<b>A</b>	<b>Appendix</b>	<b>37</b>



# Chapter 1

---

## Introduction

---

One of the main global challenges is ensuring a smooth and sustainable energy transition. Where many novel cutting-edge technologies struggle to compete and succeed in industry, solar energy has expanded vastly in both fundamental research and market production. Conversion efficiencies are consequently increased and manufacturing costs have been reduced drastically over the past decades as a result of vast research and development of photovoltaic (PV) materials and engineering of solar cells [1]. New combinations of solar architecture are increasingly important in the direction towards a sustainable future. For transportation, logistical and economical purposes, PV integration into the local architecture, buildings and rural terrains has become crucial [2]. One of the downsides of the current commercial solar cells is the dominant blue or black colour, that depreciates the cordial perception of urban construction.

Coloured PV is arising in households and smart city building integration, where aesthetics and architectural beauty play a big role. In order to achieve both functional beauty and efficiency, the research industry must develop innovative PV solutions using clever methods for coloured solar cells while preventing high efficiency losses. Over the last decades, research has not shown many coloured PV applications with complete angular and spectral control over the reflected light. Interference coatings consisting of multilayers have been used to modify the reflected spectrum, yet are not cost effective and have a strong dependency on the angle of reflection [3–5]. Thin-film silicon solar cells with semitransparent optical properties were utilised in rooftop applications, reflecting in the red wavelength regime [6]. The polymer encapsulant on top of the solar cell, however, absorbed a significant proportion of the incoming light, reducing the efficiency of the cell exceedingly.

While coloured PV has shown various concepts for building-integrated applications, the major issue remains low efficiencies. In this study, Mie-like resonators combined into metagratings are explored. The excitation of Mie resonances in subwavelength dielectric nanostructures have been studied extensively in the last decades, due to the tunable resonances and relatively low absorption compared to metallic particles. It has been shown that by tailoring the shape and refractive index of dielectric particles, it is possible to control the resonant reflection and transmission spectra [7]. Mie resonances occur through excitation of electric and magnetic modes. By altering the interferences between these specific modes, one can tune the angular distribution of the scattered light [8]. The use of Mie scatterers on planar substrates has shown tunable spectral light scattering in various colours [9–13]. Following this research, the creation of green coloured solar modules has been reported, using resonant scattering from Mie-like silicon nanoparticles [14]. With subwavelength pitches, the nanostructures of Neder et al. [14] resonantly scatter light at a tunable wavelength, while maintaining high transmission through the substrate for current generation in solar cells, losing only 10-11% in short circuit current and efficiency. Another recent publication presented a metagrating structure that scatters resonantly to a tailored angular distribution [15]. By arranging silicon Mie resonators in a periodic array spaced on top of a silver substrate, light is scattered into the first diffraction order while suppressing the zeroth order reflection. Combining multiple gratings with varying pitches, it is possible to create a Lambertian scattering profile, where the apparent brightness of the scattering is the same for an observer in every angle.



Fig. 1.1: Schematic depiction of silicon nanoparticles on a sapphire substrate.

In this thesis, we design a supercell of multiple metagratings consisting of dielectric nanoparticles that resonantly scatter according to the Lambertian cosine law, whilst transmitting the non-reflected light through a transparent substrate. First, we use Mie-like resonances in subwavelength silicon nanowires that allow us to gain spectral control over the reflected light. These resonances are tuned by optimizing the shape and spatial dimensions of the nanowires such that the scattering profile matches the desired scattering spectrum. This study realises the resonant scattering peaked around  $\lambda = 650$  nm, yielding a “red” scattering profile. Next, the nanowires are placed in multiple gratings on a sapphire substrate, that scatter light into the diffraction order following the grating equation. Fig. 1 shows a schematic overview of the metagrating. By tuning the size

---

and number of particles in different periodicities, we show that every individual grating scatters the light to the first diffraction orders. The excitation magnetic modes in silicon nanowires on a sapphire substrate enhance the scattering to the first diffraction order and destructively interfere in the specular reflection. As the pitch determines the angle of diffraction, we design a “supercell” consisting of multiple gratings that each scatter to different angles. The final design allows control of the angular and spectral response of a reflecting metasurface, while the remaining incoming spectrum is transmitted efficiently for suitable integrations in PV applications.



## Chapter 2

---

# Theory: spectral and angular control of light

---

### 2.1 Mie-like resonances

Nanophotonics covers a great variety of recent physics advancements, including the enhancement of near field effects by virtue of intermodal interferences between resonant nanostructures. While plasmonic nanostructures allow the manipulation of light at the nanoscale, only a few plasmonic applications succeeded in practice [16]. The high losses in the visible light regime and inconvenient fabrication processes needed in (opto)electronic devices are limiting the practical realization of plasmonics [17]. Recently, dielectric materials have shown strong and tunable optical Mie resonances in nanostructures with a favorable high refractive index and low optical losses, providing new and interesting opportunities for semiconductor device technologies [18].

In dielectric particles, electric and magnetic resonant modes can be optically excited with a plane wave or a dipole source. The excitation of electric dipole resonances requires the material inside the resonator to be collectively polarized by the electric field component of the incoming light, generating an electric dipole moment [7]. Magnetic dipoles, on the other hand, are driven by the coupling between the electric field of incoming light and the displacement current loops [18]. For spherical particles, these resonances are called Mie resonances, and occur when the particles diameter  $d$  approaches the wavelength  $\lambda$  adjusted by the materials refractive index  $n$ :  $2R \approx \lambda/n$ . Increasing the refractive index also increases the scattering efficiency of resonant multipoles [19–22]. Such resonances

can be observed in non-spherical particles as well, providing many opportunities for application specific designs that require particular spectral characteristic control [23]. The geometrical parameters of the individual nanoparticles can be altered such that electric and magnetic resonances can be altered both independently and interchangeably [24, 25].

In this research project, we analyse rectangular wires of height  $h$  and width  $w$ , assuming an infinite length (Fig. 2a). In order to probe the resonant behaviour of such particles, we simulate silicon nanoparticles using finite difference time domain (FDTD) simulations to optimize high scattering efficiencies for a specific wavelength range [18]. Silicon particles has been studied in many previous research developments [20, 26, 27] and are chosen here because of its high refractive index with relatively low absorption losses in the visible and infrared spectrum. We simulate the particle by illuminating it with a plane wave at zero incidence angle with the electric field component oscillating in plane as transverse electric (TE). As the 3D projection of the rectangle is assumed to be infinite, the electric modes cannot be excited and the resonances that occur in the concerning particles are purely magnetic.

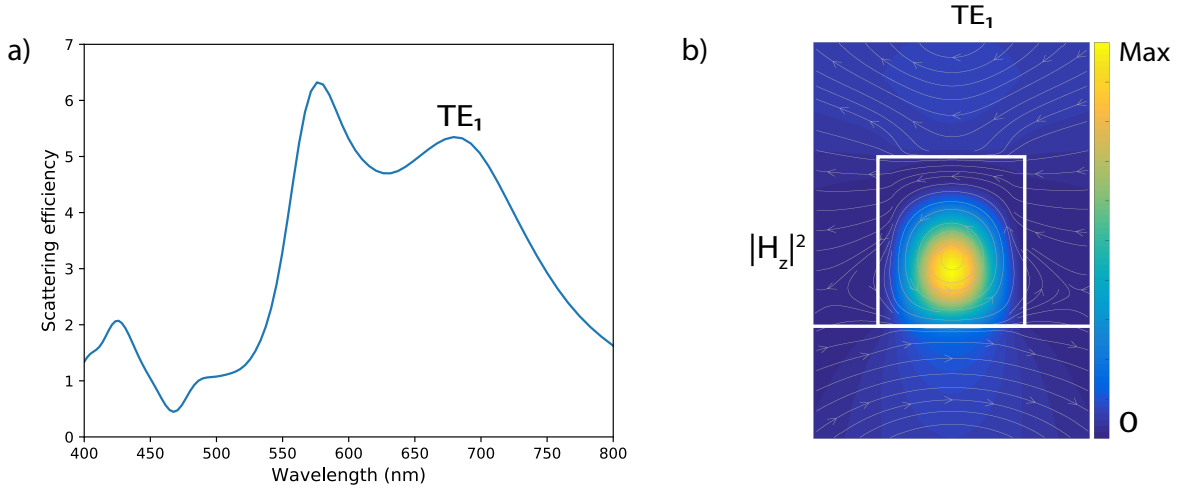


Fig. 2.1: a) Scattering efficiency of a silicon particle of height 175 nm and width 110 nm. b) Electric field lines and magnetic field strength of the resonance peak  $TE_1$ .

The scattering efficiency  $Q_{scat}$  is given by the ratio between the scattering cross section  $\sigma_{scat}$  and the geometrical cross section  $\sigma_{geo}$  [28]:

$$Q_{scat} = \frac{\sigma_{scat}}{\sigma_{geo}} \quad (2.1)$$

The scattering cross section is determined by the polarizability of the particle [7]. We identify the different modes by studying the displacement current loops and the corre-

sponding field profiles in the particle in Figure 2.1. The scattering efficiency as a function of wavelength is shown in Figure 2.1a, as well as the electric field lines (colormap is the magnetic field that is directed out of plane) of a silicon particle with a height of 175 nm and a width of 110 nm on top of a  $\text{Al}_2\text{O}_3$  substrate (Figure 2.1b). Since the electric field is oscillating in plane of the 2D simulation, the vectors of the electric field can only be directed in plane. Therefore, only the current loops of the electric field can be created, allowing only the magnetic modes to be excited. Conversely, as the magnetic field lines are directed out of plane, no magnetic loops can be created and therefore no electric modes can be excited in this setup. The light is TE polarized and the electric field profile of the highest resonance mode is shown in Figure 2.1b. At this resonant wavelength ( $\lambda = 679$  nm), the incoming electric field generates a current loop (see electric field lines in Figure 2.1b). From Maxwell's equations, it follows that a displacement current loop in the electric field generates a magnetic dipole moment directed out of plane [7]. The scattering resulting from these magnetic mode excitation accounts for the spectral reflection of the corresponding nanowire. In the next section, we discuss the optimization of the dimensions of these nanowires to attain the desired reflection spectrum.

## 2.2 Diffraction grating

In electromagnetic physical applications, layers of subwavelength particles or nanowires are often used to modify the behaviour of electromagnetic waves by introducing periodic boundary conditions [29, 30]. The sort of layers are referred to as metasurfaces. Metasurfaces have attracted considerable attention in the field of nanophotonics, where the ability to gain control over beam steering has shown promising opportunities [31]. Especially metasurfaces containing phase gradients have been researched to manipulate the reflected and transmitted wavefront of electromagnetic waves, resulting in metalenses, beam steerers, holograms and other optical device applications [32–34]. Fundamentally, these geometries are governed by the generalized laws of reflection and refraction [35], of which the reflection and transmission coefficients can be tailored such that the tangential momentum is acquired in the desired trajectory [36, 37].

In this project, we evaluate Mie-like scatterers in periodic arrays to obtain orders of diffraction. We design multiple gratings of silicon nanowires to manipulate the wave front transformation and control the outcoupling of light into the desired diffraction orders. The nanowires are illuminated with a TE plane wave at normal incidence. The periodicity of the grating is chosen to be larger than the resonance wavelength of the scattering profile. When particles are spaced with a periodicity  $p$  larger than the wavelength  $\lambda$ , diffraction

occurs, following the diffraction grating equation

$$p \sin \theta = \frac{m}{n} \lambda, \quad (2.2)$$

where  $\theta$  is the angle of diffraction,  $m$  is the order of diffraction and  $n$  is the refractive index of the material where the diffraction occurs. A schematic overview of the diffraction within the metasurface is given in Figure 2.2. The grating is designed such that the reflected wavefronts are at resonance. In this study, we design nanowires on top of a sapphire substrate that consequently reflect light in air. Therefore,  $n = 1$  and diffraction occurs when  $p \sin \theta = m\lambda$ . The first order diffraction channels ( $m = 1$ ) arise when  $p > \lambda$ . The metasurface is designed to scatter at a resonance wavelength of  $\lambda = 650$  nm. According to the grating equation, first order diffraction occurs for pitches varying for  $650 \text{ nm} < p < 1300$  nm. Above  $p = 1300$  nm, the second order diffraction occurs, and light is reflected in five channels ( $-2, -1, 0, 1, 2$ ) instead of three ( $-1, 0, 1$ ). For a fixed  $\lambda$  and  $n$ , the pitch determines the outgoing angle of diffraction. In the desired range of pitches, the first order diffraction angles range from ( $30^\circ$ - $90^\circ$ ). Rooftops generally have an angle of about  $40^\circ$ . Therefore, the interest of the angular distribution lies in large angle scattering ( $30^\circ$ - $75^\circ$ ) such that light is reflected correctly to an observer on the street.

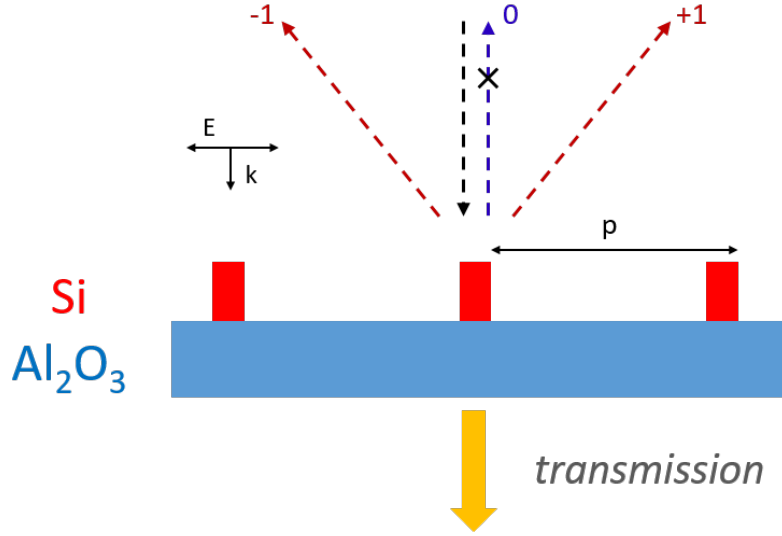


Fig. 2.2: Silicon particles spaced a pitch  $p$  on a sapphire substrate open up diffraction channels. Normal incidence TE light reflects into the  $-1, 0, +1$  orders and transmits the remaining light into the substrate. The zeroth order is reduced while first order is enhanced.

Ultimately, the resonant reflected light should be directed from the rooftop to the street. In other words, the angular distribution should cover only the large angles ( $30^\circ$ - $75^\circ$ ). Simultaneously, light should not be reflected in other angles. In the given symmetri-

cal design of such gratings, light is reflected into both first diffraction orders as well as the zeroth order. For preliminary research purposes, the metasurface is designed to scatter to both diffraction orders (due to symmetry) while reducing the reflection to the zeroth order. The latter aspect is not a pure optimization but rather a material characteristic consequence. Whereas the silicon nanowires scatter light into the zeroth order according to the grating equation, the sapphire substrate reflects a proportion of the incoming light due to its refractive index. We do not explicitly show this, but we assume that the phase difference between the sapphire reflection and the scattering of the nanowires accounts for partly destructive interference in the specular reflection. Therefore, the zeroth order reflection is reduced significantly, as will be shown in Chapter 3.

## 2.3 Lambertian scattering

A complete system of photometric quantities and principles was established by Johann Heinrich Lambert in 1779, which were generally used to determine illumination intensities and to quantify features of human vision. Lambert had been interested in optical properties of light for a long time. He looked at three qualitative observational statements about light intensity and transformed them into independent quantitative laws that he could use to set up a brightness scale. The third law states: “Intensity of light varies as the cosine of the angle of incidence of light upon the object viewed” [38]. In other words, for the human eye, the surface has the same apparent brightness when viewed from any angle. As the emitted radiation  $I$  from a certain area  $dA$  is reduced by the cosine of the outgoing angle  $d\theta$ , the solid angle  $d\Omega$ , subtended by the visible surface of the observer, is reduced by the same amount (Figure 2.3). Therefore, the radiance in every angle is the same. The goal of our design is to reach such a Lambertian scattering profile, because an observer can then perceive the colour of the potential solar cell the same in every angle.

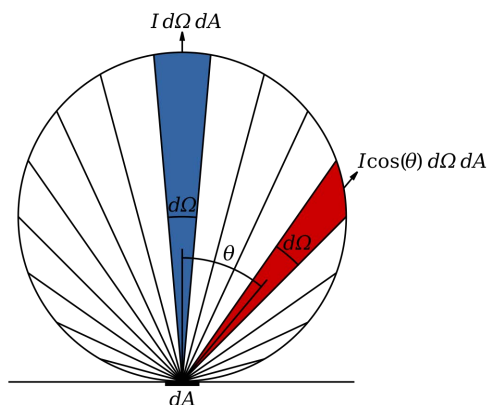


Fig. 2.3: Lambertian cosine law; the intensity  $I$  of an area  $dA$  into every solid angle  $d\Omega$  follows the  $\cos\theta$ .



## Optimization and design

---

### 3.1 Time-domain modeling by FDTD

#### 3.1.1 Setup and analysis

In this chapter, the optimization steps through numerical simulations in Lumerical are discussed thoroughly. For all simulations, the Finite-difference time-domain (FDTD) method has been used in a 2 dimensional (2D) grid. In this method, time is discretized in steps, allowing a plane wave to start at an initial time and the solutions of the physical problem are computed iteratively. The optical response in the frequency domain is then found through the Fourier transformation of the time domain solution.

The simulation setup is as follows: a single 2D silicon nanoparticle is placed on an infinite sapphire substrate in a Perfectly Matched Layer (PML) setup. For illumination, a plane wave source is used, with the electric field component oscillating parallel to the width of the particle. A frequency domain field and power monitor is placed around the particle to obtain the spatial and temporal electric and magnetic field components of the incoming and scattered wavefront, along with the scattering cross section. It has been shown that the electric and magnetic fields that arise at the given resonance frequencies can be correlated to the excitation of specific modes inside the particle [7]. The excitation of such a mode allows the incoming light to be scattered resonantly according to the scattering profile of the corresponding mode. The Mie-like resonances depend on the dimensions of the nanoparticles and on the refractive index of the particle and the substrate. This study involved a high index material (Si) to obtain high resonance scattering profiles and a low index substrate ( $\text{Al}_2\text{O}_3$ ) to allow light to pass through the

material such that the transmitted light can be collected in the solar cell underneath the fabricated layer. The optical constants of the silicon and sapphire materials used in these simulations are taken from Palik [39].

The dimensions of the particle, height and width, are optimized to scatter light at a resonance wavelength of  $\lambda = 650$  nm to obtain a “red” scattering profile. We simulate the same particle in periodic boundary conditions with a chosen pitch  $p$  (determined below). By performing multiple simulations while varying the height and the width of the particle, the reflection into the diffraction orders is collected by a grating transmission monitor. The percentage of the incoming power that is reflected to the +1 and -1 orders is given in Figure 3.1a, for height  $h = 175$  nm and pitch  $p = 1100$  nm. Varying the width changes the resonances in the particle. A clear trend can be observed in the higher wavelength range from 500 to 800 nm, where a greater width results in a higher resonance wavelength. As the dimensions of the particle increase, the displacement current loops that shape the magnetic resonance increase as well, resulting in a higher resonance wavelength. For even higher widths, the higher order resonance modes can be excited as well, yielding the high first order reflection in the 400 to 600 nm wavelength range.

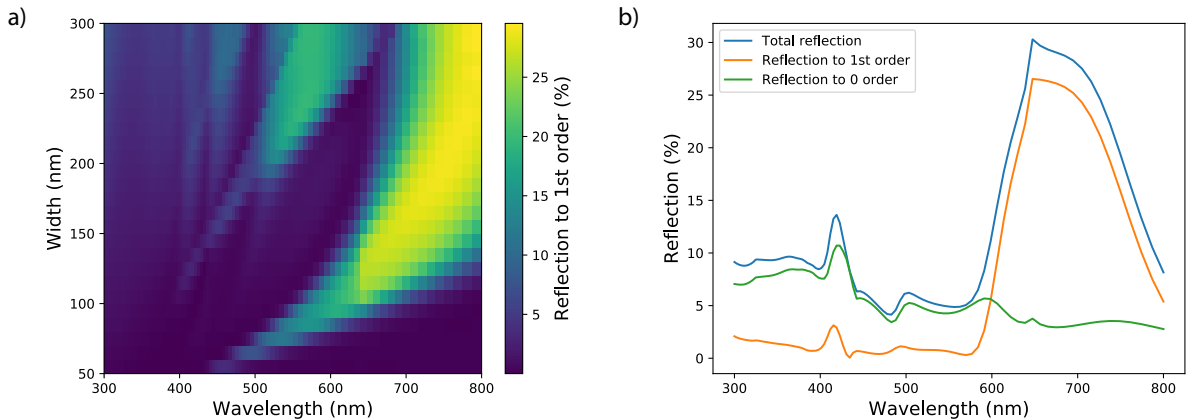


Fig. 3.1: a) Total reflection to the +1 and -1 order for varying width and wavelength; increasing the width of the particle increases the resonance wavelength. b) Total reflection (blue), enhanced reflection to the +1 and -1 order (orange) and reduced reflection to the 0 order (green) for  $w = 110$  nm.

The total reflection to the first order is highest at around 650 nm, at a width of 120 nm. Figure 3.1b shows the reflection spectrum to the first order (orange curve) for a particle with dimensions width  $w = 120$  nm, height  $h = 175$  nm and pitch  $p = 1100$  nm. The first order reflection is enhanced compared to the zeroth order reflection (green curve). The major portion of the reflection in the green and blue part of the visible spectrum is a consequence of the direct reflection of the sapphire substrate, which is

around 8% for the given wavelength range. A clear peak at 410 nm is observed. This is a resonance peak occurring from a higher order mode excitation. The high peak in the first order reflection is the result of the high resonant scattering at the red part of the visible range. The majority of the reflected light is scattered into the first order ( $\sim 26\%$ ) and while the reflection is reduced in the zeroth order ( $\sim 4\%$ ). Therefore, in a grating with particles spaced  $p = 1100$  nm apart, the diffraction of the array of particles steers the reflected light to the +1 and -1 order. According to the grating equation

$$p \sin \theta = \frac{m}{n} \lambda \quad (3.1)$$

it follows that for a pitch of  $p = 1100$  and a wavelength of  $\lambda = 650$  nm, the outgoing angle of the first diffraction order is  $\pm 36^\circ$ . In the next section, we discuss this optimization for multiple pitches.

## 3.2 Large angle scattering

### 3.2.1 Single particle in periodic boundary conditions

The goal of these FDTD optimizations is to determine the wavelength bandwidth that should be reflected into the desired reflected angles. This process of optimizing the resonance wavelength of a specific grating can be done for multiple gratings as the pitch is varied. For a given wavelength  $\lambda$ , fixed refractive index  $n$  and at normal incidence, the first order diffraction angle is determined by solely the pitch. The bandwidth should ideally be narrow for high external quantum efficiencies in the solar cell. However, the human eye retrieves light as information through specific cones. These cones have wavelength dependent sensitivities with a peak wavelength range of around 20 nm [40]. In order to take this sensitivity into account, we broaden the peak range and optimize the reflection for a bandwidth of 630-670 nm. In the simulation, we keep the height constant ( $h = 175$  nm) for the ease of fabrication purposes. Next, we vary the width of the particles as well as the pitch by simulating a single particle of width  $w$  in a FDTD simulation with periodic boundary conditions of period  $p$ . We excite the particle with a plane wave source and monitor the reflection to the diffraction orders (-1,0,1). From the grating equation, it follows that in this setup, the pitch determines the outgoing angle of diffraction. The motivation of this design was to obtain large angle scattering from 30-75°. For a wavelength of  $\lambda = 650$  nm, this results in a range of pitches from 1300 nm (30°) to 675 nm (75°). Therefore, the width is varied from 70 nm to 200 nm and the pitch is varied from 675 to 1300 nm.

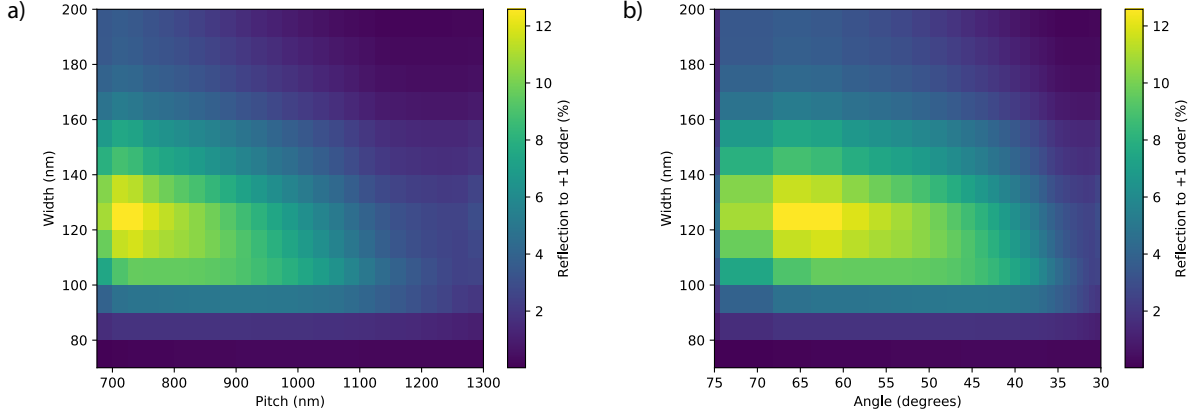


Fig. 3.2: Reflection to the +1 order, averaged over wavelengths 630-670 nm with a) varying width and pitch b) varying width and outgoing angle.

Figure 3.2 shows the result of varying the mentioned parameters, where every pixel shows the reflection to the first order averaged over the wavelength bandwidth of 630-670 nm. In the simulation result, we observe that the first order reflection decreases with the increasing pitch. As the pitch increases, the outgoing angle decreases and the scattered light is going more into the zeroth order, therefore reducing the first order reflection. We can optimize the design by choosing the width of the particle for each pitch, according to the highest reflection percentage to the first order. In this way, we obtain values for the width and first order reflection at every pitch. Since different widths are used to optimize the first order reflection, the resonances are slightly different, resulting in a broader resonance peak (see Figure 3.4b).

### 3.2.2 Designing the unit cell

Subsequently, the design is made by placing multiple gratings next to each other, creating a varying periodic array of silicon nanowires. The design is created according to the Lambertian cosine law in 2D (see Section 2.4), where the scattered light into every angle follows the  $\cos \theta$  as follows:

$$\frac{n_i p_i R_i}{n_0 p_0 R_0} = \cos \theta \quad (3.2)$$

where  $n_i$  is the number of particles in grating  $i$ ,  $p_i$  is the pitch in grating  $i$ ,  $R_i$  is the first order reflection in grating  $i$  and  $n_0, p_0, R_0$  are the number of particles, pitch and first order reflection in the first grating with the lowest pitch respectively. An arbitrary total number of 25 gratings was chosen such that each subsequent grating scatters to at least one degree higher. As a result, the scattering angles originating from the varying pitches range from 30-75°. From Figure 3.2 we observe the the reflection decreases for higher

itches. Therefore, in order to scatter according to the Lambertian cosine law, the number of particles in high pitch gratings needs to be increased. Consequently, for fabrication purposes, the design was made such that for higher pitches, the subsequent gratings scatter with more than one degree difference (see Appendix A for design parameters). Each grating contains  $n_i$  particles with a pitch  $p_i$ , resulting in an area of  $A_i = n_i * p_i$ . The total area of the unit cell is the sum of all grating areas  $A_i$ , and adds up to  $223 \mu\text{m}$  for this large angle scattering design. A schematic overview of the design, resulting in unit cell that scatters from  $30\text{-}75^\circ$ , is presented in Figure 3.3. It was chosen to design the unit cell with a gradually increasing pitch, to obtain a clear structure and noticeable design. However, since the neighbouring gratings in this case scatter to almost the same angle, the interference is relatively large between gratings. Therefore, it would be better for future applications to place the large pitch gratings next to small pitch gratings.

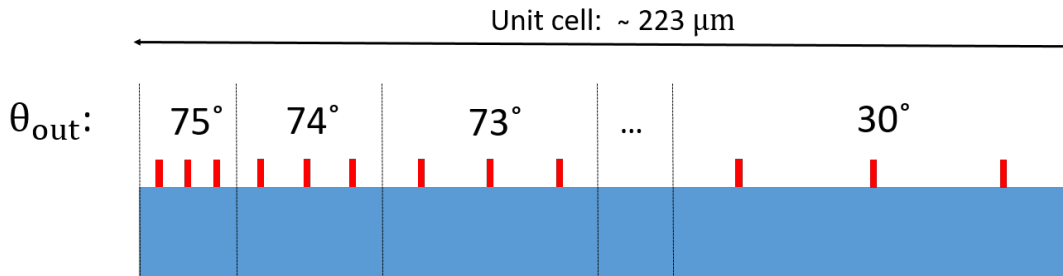


Fig. 3.3: Unit cell of the design containing 25 different gratings with varying pitches from  $675 \text{ nm}$  ( $75^\circ$ ) to  $1300 \text{ nm}$  ( $30^\circ$ ). The number of particles in each grating is purely schematic here; see Appendix A for actual number of particles per grating. This results in a total area of  $223 \mu\text{m}$ .

### 3.2.3 Spectral response of the unit cell

Following the parameter optimization, we have obtained the unit cell design and can now simulate and evaluate the optical response. First, we analyse the spectral first order reflection for each specific grating with periodic boundary conditions. An FDTD simulation with a single silicon particle is again placed on a sapphire substrate with a pitch of  $p_i$ . A reflection monitor is used to obtain the reflected spectrum into the first order and is presented in Figure 3.4a for pitches  $700\text{-}1300 \text{ nm}$ . We observe a broad peak from  $600\text{-}800 \text{ nm}$  for almost all pitches. This is a result of the Mie-like resonances inside the particle that scatter into the diffraction order following the grating equation. We designed the broad peak to be at resonance around  $\lambda = 650 \text{ nm}$  to obtain a “reddish” scattering profile. For lower wavelengths, the first order reflection is close to zero. There are two peaks occurring at around  $530 \text{ nm}$  and  $420 \text{ nm}$ . These peaks correspond to the

scattering of higher order mode resonances inside the particle (see Fig. 2.1). Another feature that we have seen and explained before, is the decrease in reflection for increasing pitch. The redshift in the reflection peak for higher pitches is due to the broadening of the excited resonance modes. Therefore, we obtain reflection percentages from 4% ( $p = 1300$ ) to 11% ( $p = 700$ ). The final feature shows zero reflection for certain pitches at high wavelengths. When the wavelength exceeds the pitch, the grating equation does not hold anymore, and no diffraction can physically take place. Therefore, the reflection to the first order is zero for every  $\lambda > p_i$ . Since the total response of the unit cell is of our interest, we take the weighted average of all gratings, taking into account the relative area per grating. This averaged reflection to the first order is shown in Figure 3.4b. A clear enhanced broad peak is observed at 600-800 nm, yielding 8% reflection in this wavelength range.

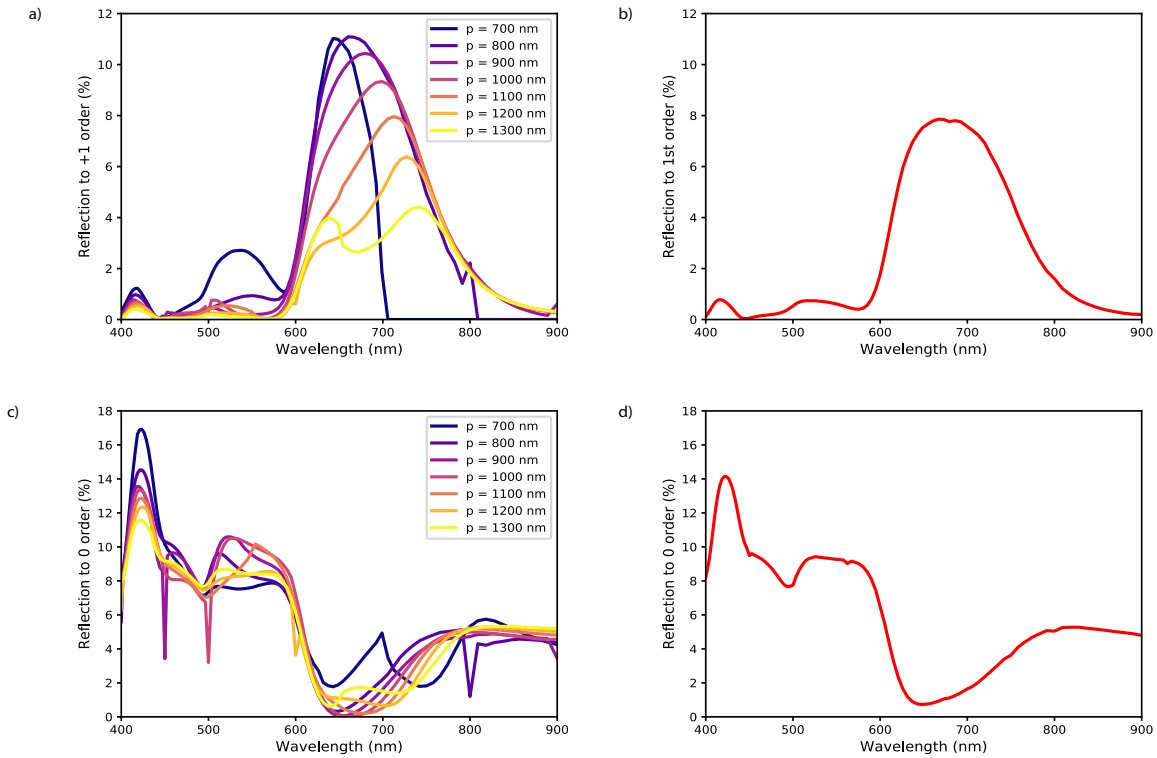


Fig. 3.4: a) Reflection to the +1 order for varying pitch b) Reflection to the +1 order, averaged over all gratings c) Reflection to the 0 order for varying pitch b) Reflection to the 0 order, averaged over all gratings.

A similar analysis is shown for the zeroth order reflection in Figure 3.4c. In the wavelength range where the first order reflection is peaked, the zeroth order reflection is reduced to almost zero. The particles were designed to scatter most of the light into

the first diffraction order while cancelling the zeroth order in a desired wavelength range. This is what we observe in Figure 3.4c. In the lower wavelength range, the reflection to the zeroth order is around 8-10%, which is mainly a result of the characteristic reflection spectrum of the sapphire substrate. Again, the two peaks at 530 nm and 420 nm are a result of the higher order modes scattering into both the zeroth and the first order diffraction channels. Furthermore, the reflection to the zeroth order is averaged similarly as in Figure 3.4b. Comparing the averaged first order reflection to the averaged zeroth order reflection, it is clearly observed that the peak in the first order coincides spectrally with the dip in the zeroth order, confirming the desired scattering profile.

### 3.2.4 Angular response of the unit cell

The reflection that is shown in Figure 3b is the total reflection of the first order averaged over all angles. In order to reveal the angular distribution of this reflection spectrum, we simulate the full unit cell in an FDTD simulation with PMLs. A plane wave source is used to excite the unit cell and a grating monitor is used to calculate the reflection of the unit cell per angle. Over a wavelength range of 560-700 nm, the angular distribution of the relative reflection per degree is shown in Figure 3.5a. Ultimately, the angular distribution should look Lambertian. That is, the intensity per angle should follow the cosine of that angle. The unit cell is designed to scatter light in the diffraction angles from 30-75°. Although the first order diffraction is scattering to these angles, light is not completely cancelled in the zeroth order. Consequently, Figure 3.5a shows a high relative reflection per degree at 0 degrees, as in every grating a small percentage of the incoming light is reflected into the zeroth order. The design was optimized to have diffraction into the desired angles at a wavelength of 650 nm. Correspondingly, the reflection is zero for all angles other than 0° and 30-75°. For lower wavelengths, the grating equation opens up higher order diffraction channels that scatter to higher angles. This can be seen in the high absolute angles in this figure, where a second order diffraction appears below  $\lambda = 650$  nm. Another slightly noticeable feature reveals a gradient where for higher wavelengths, the reflection goes to higher angles. Similarly, this can be explained by the grating equation  $p \sin \theta = \frac{m}{n} \lambda$ . For an equal pitch  $p$ , diffraction order  $m$  and refractive index  $n$ , increasing the wavelength scales increasingly with  $\sin(\theta)$ .

In order to analyse whether the angular distribution follows the desired cosine law, the relative reflection per degree is plotted for a single wavelength  $\lambda = 650$  nm in Figure 3.5b. The blue part of the reflection represents the zeroth order reflection and goes out of scale. The real value of the zeroth order reflection is 0.65% per degree. The grey dashed line shows the  $\cos(\theta)$  distribution in this angle range. Accordingly, the results

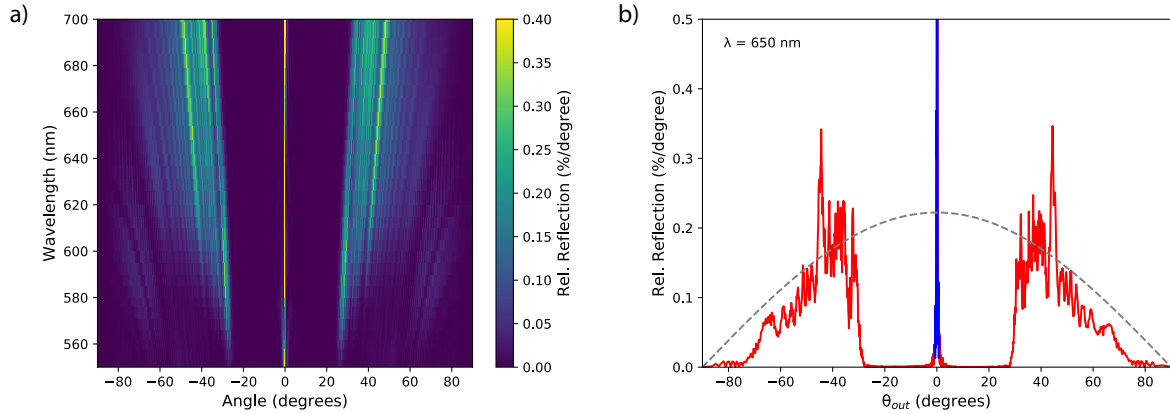


Fig. 3.5: a) Relative reflection per degree in the wavelength range 550-700 nm and angular range  $-90^\circ$  to  $90^\circ$ . b) Relative reflection per degree for  $\lambda = 650$  nm and angular range  $-90^\circ$  to  $90^\circ$ . Zeroth order reflection goes out of scale (blue), other angles of reflection (red) are plotted against  $\cos \theta$  (grey dashed).

(red) follow the cosine law (grey) significantly in the range of  $30^\circ - 75^\circ$ . There is an outlier at  $\pm 45^\circ$ , which was only later identified as a calculation error. In designing the unit cell, a miscalculation in the number of particles amounted to a higher reflection percentage in this grating. In simultaneous simulation and fabrication, the calculation process was not repeated to eliminate this error. As we will see in Section 5.2, fabrication yields the same calculation error as in the simulation. This design is therefore the full unit cell design that will further be used for fabrication and measurements in the succeeding sections.

## Fabrication

### 4.1 Fabrication steps of the supercell

Following the optimization and final design of the previous section, the next step is to fabricate the desired unit cell. Before fabricating the unit cell, we make a “supercell” design consisting of six unit cells in order to obtain a field that extends the spot size of the laser used in experiments (see Section 5.1). The length of the “supercell” is then designed to an area of 1.34 x 1.5 mm and is fabricated accordingly. The fabrication process of the “supercell” is given in Figure 4.1.

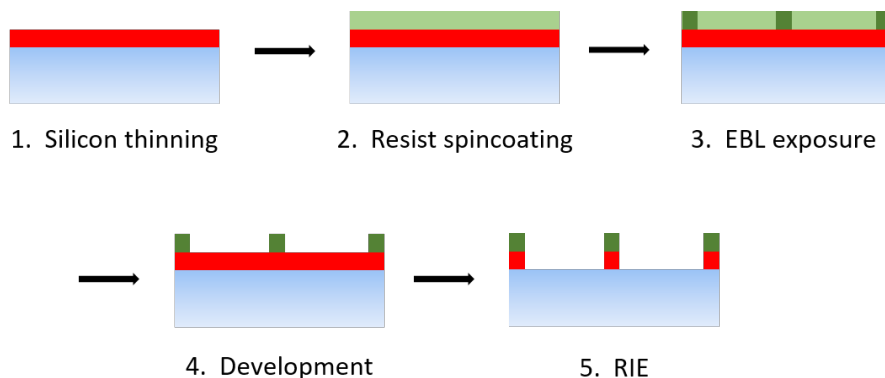


Fig. 4.1: Fabrication steps: 1. Silicon thinning using reactive ion etching (RIE) 2. Spincoating negative resist (HSQ) 3. Electron beam lithography (EBL) 4. Development of resist 5. RIE.

Initially, we start with 1x1 cm silicon-on-sapphire substrates (500nm c-Si on 0.46mm R-plane sapphire, MTI Corporation). The silicon is etched down to a thickness of 175 nm using reactive ion etching (RIE) in a HBr<sub>2</sub> (48.5 sccm) and O<sub>2</sub> (1.5 sccm) plasma (see

RIE etch recipes in Appendix A). Next, the wafer was spin-coated at 4000 rpm for 45 seconds with HSQ, a high resolution negative resist, and baked for 150 seconds at 180°C. The resist layer had a thickness of 50-60 nm. After cooling down the HSQ, Electra 92 (AR-PC-5091) was spin-coated at 2500 rpm for 45 seconds and baked at 120 seconds at 90°C to obtain better conductivity of the sample. The substrate is then exposed by electron beam lithography (EBL) using a dose of 2400  $\mu\text{C}/\text{cm}^2$ . After patterning the sample, it is rinsed in water for 30 seconds to remove the Electra and then developed in TMAH for 75 seconds at 50°, rinsed in water for 15 seconds and finally rinsed in IPA for 15 seconds. The patterned sample is then etched using RIE in two subsequent etching runs (Fig 4.2ab). In the first run, a chlorine ( $\text{Cl}_2$ ) step for 20 seconds at 60° is used to etch away the native oxide layer. In the second step, the sample is etched in a  $\text{HBr}_2$  (48.6 sccm) and  $\text{O}_2$  (1.4 sccm) plasma at 60° for 27 seconds. In order to precisely etch down the silicon, the etch steps were divided into two steps for silicon. The second etch time was 5 seconds to etch away the remaining silicon layer (57 nm). After these fabrication steps, the sample consists of silicon nanowires with a remaining HSQ layer on top, on a sapphire substrate. The HSQ is not removed as this process involves chemical reactions that also react with the sapphire substrate. It is not expected to have a great influence in the spectral response, but it could account for the dissimilarities in the results (Chapter 5).

parameter	value
$\text{Cl}_2$ gas flow [sccm]	50
pressure [mTorr]	7
Set temperature [°C]	60/61
HF/RIE forward power [W]	30
ICP forward power [W]	750
time [s]	20
etch rate [nm/sec]	~2.0
DC Bias to be expected [V]	150

parameter	value
HBr gas flow [sccm]	48.6
$\text{O}_2$ gas flow [sccm]	1.4
pressure [mTorr]	7
Set temperature [°C]	60/61
HF/RIE forward power [W]	30
ICP forward power [W]	750
time [s]	27
etch rate [nm/min]	~2.9
DC Bias to be expected [V]	155

Fig. 4.2: a)  $\text{Cl}_2$  recipe parameters b)  $\text{HBr} + \text{O}_2$  recipe parameters.

## 4.2 SEM images of the fabricated supercell

A top image and tilted top image of the sample is taken by a scanning electron microscope (SEM), and are shown in Figure 4.3ab. The pictured line is a nanowire in the grating with pitch 700 which was simulated to have a width of 120 nm. We observe fairly straight nanowires of the correct height (175 nm) and width (120 nm). Sapphire is a transparent substrate with very low conductivity. Therefore, a layer of Electra 92 is spincoated on top of the sample to increase conductivity needed for imaging in the SEM. The roughness on the side of the nanowires is due to this additional layer and was only placed for imaging. In the experiments there was no Electra 92 on top. Figure 4.3c shows a top view of an individual grating consisting of 16 nanowires each spaced a pitch of 1200 nm apart. The SEM image shows fairly straight lines with pitches exactly as simulated.

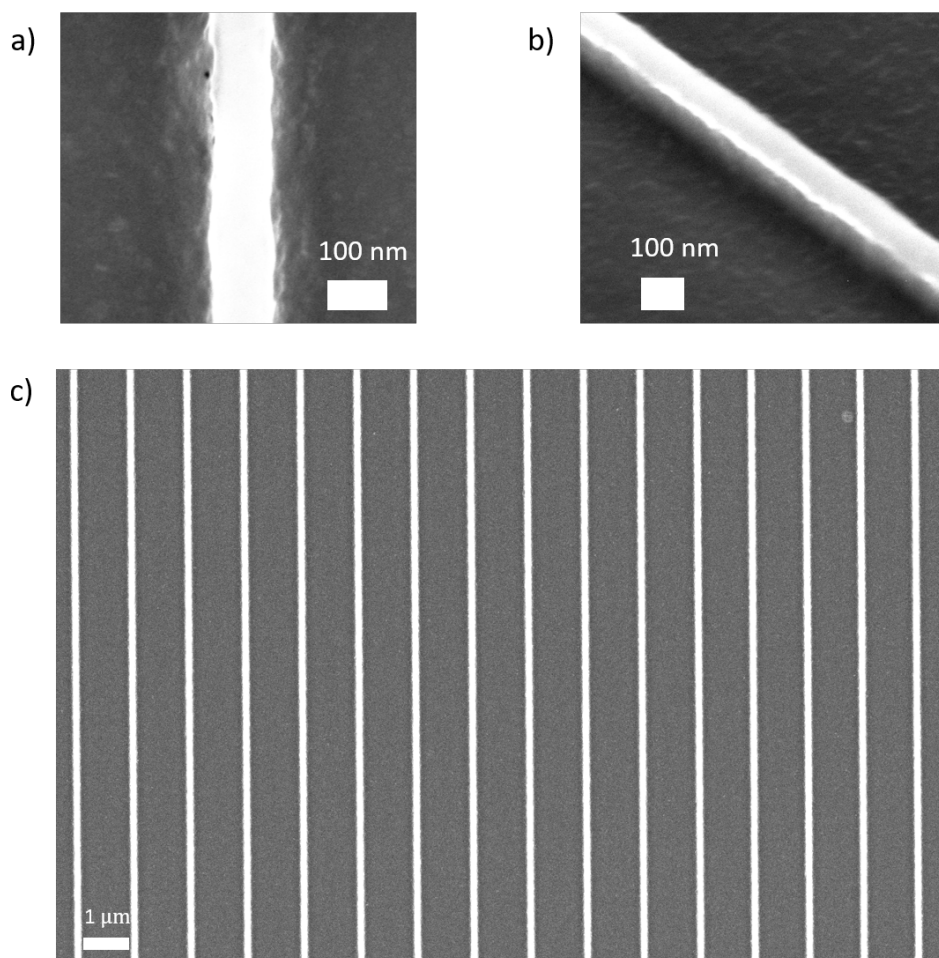


Fig. 4.3: SEM images of the fabricated sample. a) Top view of a single nanowire of  $w = 120$  nm b) Tilted image of a single nanowire (tilt angle is  $40^\circ$ ) c) Top view of a grating consisting of 16 particles with a pitch of 1200 nm.

Figure 4.4 shows a full unit cell, depicted by the red dashed line. Starting with a high pitch grating on the left part of the SEM image, the subsequent gratings gradually change with decreasing pitch to the right part of the image. To the right of the red dashed line, a new unit cell starts, and a clear difference in pitch can be observed. In general, the nanowires are fairly straight and the pitch of the nanowires is very accurate. The main challenges of this fabrication procedure were fine tuning the etching rates of silicon on sapphire and determining the right combination of the resist and the dose for EBL.

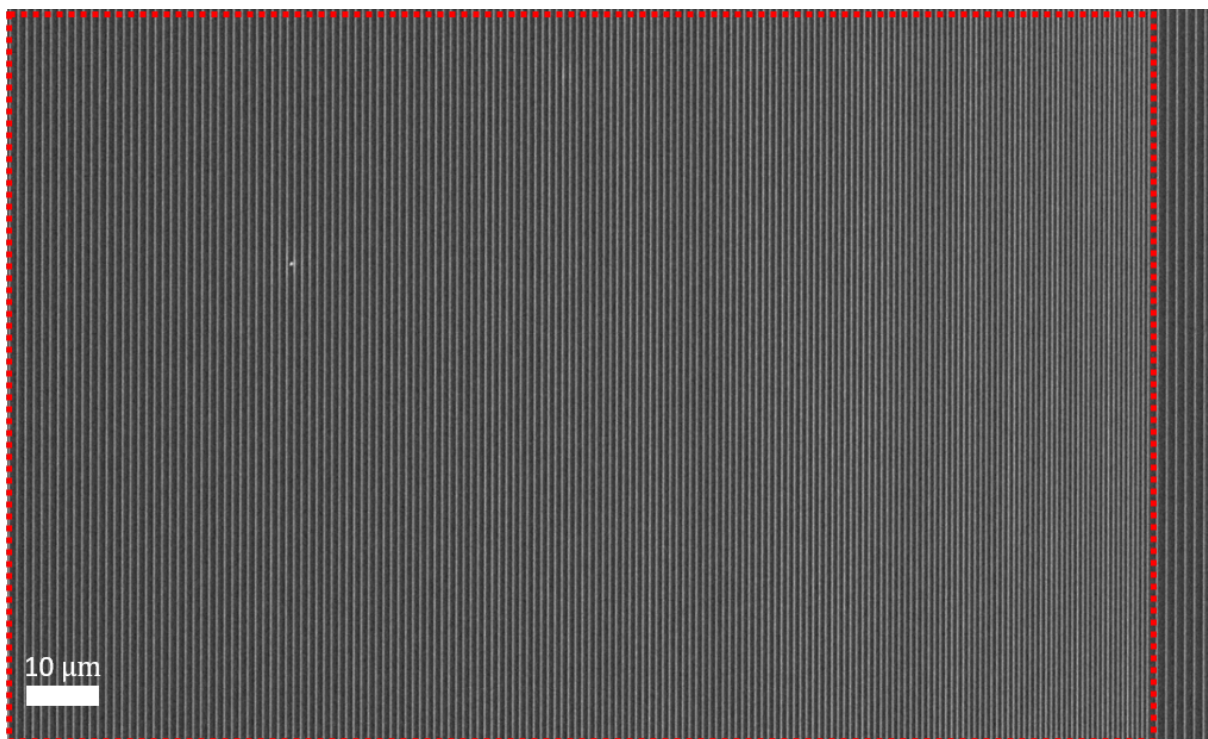


Fig. 4.4: SEM of the full unit cell (dashed red line) containing all gratings with varying pitch. Stitching of the unit cells can be seen on the right hand side of the SEM image.

## Chapter 5

---

# Optical measurements of large angle scattering

---

In this section, we experimentally demonstrate the spectral and angular response of the fabricated cell. First, we analyse the reflection spectrum to observe the total first and zeroth order response of the scattering. Correspondingly, the transmission spectrum is measured to illustrate the applicable use of a transmissive substrate in future solar cells. Next, we measure the reflection in every angle to confirm the desired scattering profile at the resonance wavelength. As the simulations were performed in two dimensions using a plane wave excitation with an oscillating electric field perpendicular to the nanowires, the experimental setup has to account for this. Therefore, we use a polarizer in all setups and position the sample such that the incoming light also has the electric field oscillating perpendicular to the long axis of the nanowires. It is important to note that this setup contains polarized light, in contrary to the possible solar cell application, where the illumination is unpolarized sunlight (see Chapter 6 for discussion).

### 5.1 Spectral response: integrating sphere

The spectral response of the sample is measured using an integrating sphere (Figure 5.1). There are two methods of measurements; a reflection spectrum with a non tilted and a tilted sample. In the former method (“Setup 1”), the sample is placed perpendicular to the incoming light at the back of the integrating sphere (Figure 5.1a). The incoming white light is then reflected and transmitted by the sample. Since the sample is perpendicular

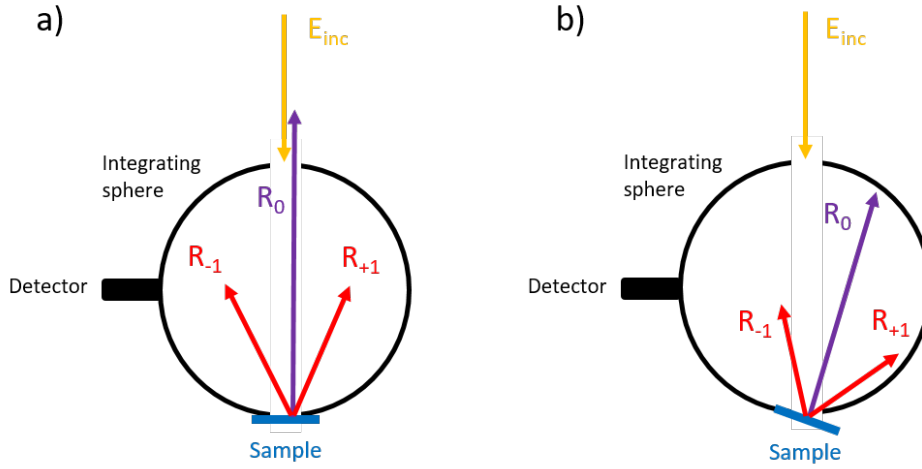


Fig. 5.1: Integrating sphere setup with normal incidence light on a) non tilted sample; zeroth order reflection not detected b) tilted sample; zeroth and first order reflection detected.

to the incoming light, the specular reflection exits the integrating sphere at the location where it entered, and is therefore not collected in the measurement. All the remaining reflected light is scattered within the sphere until it is collected at the photodetector. Note that the detector is actually on top of the integrating sphere, only pictured here on the side. The diffraction occurs in the plane perpendicular to the nanowires and is therefore always indirectly detected through the scattering in the integrating sphere.

The second method (“Setup 2”) involves a tilted sample at the back of the sphere, where ultimately the specular reflection is also collected by the detector (Figure 5.1b). For this reason, the second method includes both the first and zeroth order diffraction, while the first method only measures the first order diffraction. The difference between the two measurements therefore yields solely the zeroth order reflection.

As the white light laser has a specific spectrum intensity, the total white light reflection is measured as the reference. Furthermore, the measurement includes optical intensity noise that needs to be accounted for. First, the nanowires are fabricated on a transmissive substrate, allowing light to partially enter the sphere through the back of the substrate. Secondly, the detection precision is not perfect and also encounters some intensity noise. This background noise is also taken into account in the measurements.

### 5.1.1 First and zeroth order reflection

To demonstrate the similarities between the optimized simulations and the measurements of the fabricated sample, Figure 5.2 shows both first and zeroth order reflection spectra for simulations and measurements. As we mentioned before, the reflection percentages

are referenced by the white light of the laser and the background is subtracted. In Setup 1, the reflection spectrum of the sample is measured without the zeroth order reflection. As a result, only the first order reflection of the whole sample is measured and presented in Figure 5.2b. The broad banded peak in the first order reflection is centered at a wavelength of  $\lambda = 614$  nm and yields 9.9% reflection. The bandwidth of this spectrum is around 200 nm, which is in accordance with the simulation bandwidth represented in Figure 5.2a. The spectral response is slightly higher ( $\sim 2\%$ ) over the whole wavelength range. One explanation for this artifact is the presence of the negative resist HSQ that is still on top of the silicon nanowires. Therefore, it is important in future research that this is explored further with and without resist. In the higher wavelength range, above 750 nm, the reflection to the first order is higher than in simulations. Furthermore, the edges of the broad peak are not as steep as in simulation. This is mainly due to fabrication imperfections. As the nanowires are not perfectly straight in fabrication, the resonances are not as specific and enhanced as in simulation, yielding a more gradual increasing and decreasing peak.

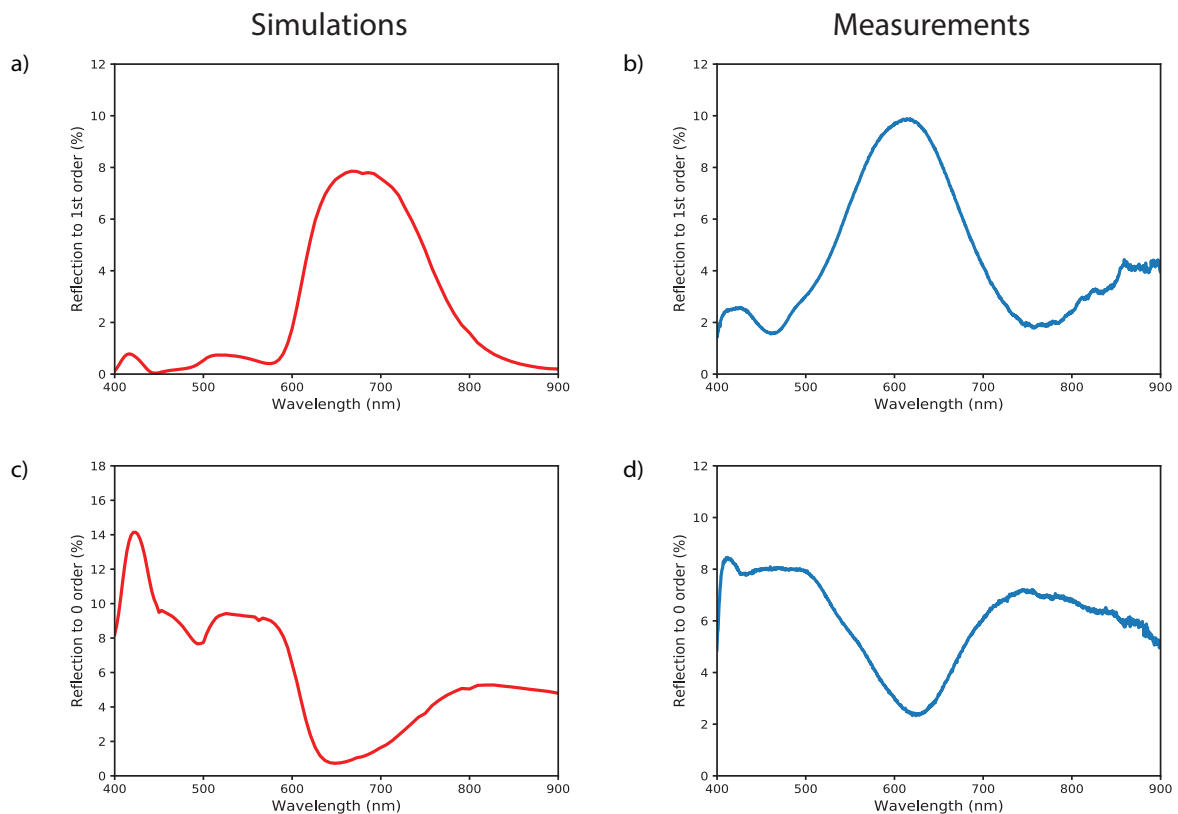


Fig. 5.2: a) Simulated reflection spectrum to the first order b) Measured reflection spectrum to the first order c) Simulated reflection spectrum to the zeroth order d) Measured reflection spectrum to the zeroth order.

Next, we analyse the zeroth order reflection, given in Figure 5.2cd. The zeroth order reflection is calculated by taking the reflection spectrum of Setup 2 and subtracting the reflection spectrum in Setup 1. Experimentally, we show that at the broad resonance around  $\lambda = 614$  nm, the zeroth order reflection is reduced. Similarly to the simulation results, the zeroth order reflection is around 8% in the lower wavelength range and decreases to 2% at the resonance. Additionally, the reflection at wavelengths above the resonance is decreasing slightly, similar to the simulation. Given the minor differences in simulation and experimental results, we can say that the fabricated sample well represents the expected reflection spectra, both for the zeroth and first order reflection.

## 5.2 Angular response: rotating stage

In the previous section, we experimentally demonstrated the spectral response confirming the theoretical expectations. The next challenge was to show that the designed grating of nanowires has an angular distribution that follows the cosine law. For this experiment, a rotating stage is used to measure the angular response of the “supercell”. The setup is given in Figure 5.3. In the center of the setup, there is a sample holder which can be rotated separately. The outer ring of the setup holds a power meter, which can be rotated on the ring per one degree. The sample is illuminated by a monochromated supercontinuum laser, where each measurement is performed for a specific wavelength. The detector on the rotation stage is a power meter that collects the intensity of the reflected light with an aperture of one degree. The path of the source is coming in from slightly upwards, such that the sample reflects the zeroth order to the power meter as well. This slight tilt suggests that the incoming light is not at normal incidence. However, the sample consists of nanowires that are illuminated through the polarizer where the electric field is oscillating perpendicular to the particle. Therefore, the incoming angle is still at normal incidence in the plane perpendicular to the sample. The measurements are performed such that at every wavelength, the detector measures the reflected intensity at every angle from  $-90^\circ$  to  $90^\circ$ .

### 5.2.1 Reflection to every angle

In Section 3.2.4 we theoretically simulated the “supercell” and showed the angular response for a wavelength range from 550-700 nm. For comparison, the same results are shown in Figure 5.4ac. The measurements were performed in the same wavelength range with steps of 10 nm. Figure 5.4b shows the relative reflection per degree for the desired wavelengths. There are a number of features in the experimental results that confirm

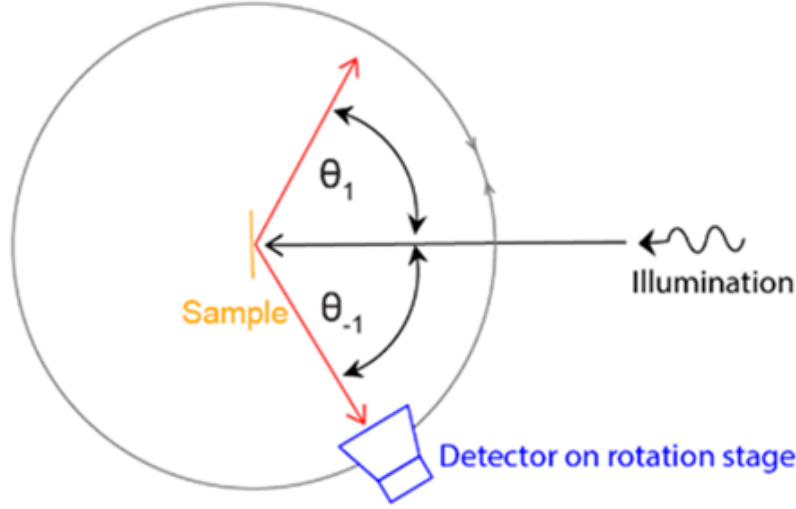


Fig. 5.3: Rotating stage setup: monochromated light is incoming at normal incidence, the power meter rotates around sample to collect the reflected intensity at every one degree. (Re-adopted from Neder et al. [15]).

the theoretical predictions. First of all, it is apparent that the sample does not scatter to angles below  $30^\circ$  and above  $75^\circ$ . Therefore, all gratings within the sample scatter to the designed diffraction orders conveniently. Secondly, as the design was optimized to only have a first diffraction order for a wavelength of  $\lambda = 650$  nm or higher, the measurements realize this goal. Below  $\lambda = 650$ , a clear second order of diffraction appears correspondingly with the simulations. Furthermore, a slight gradient is observed where for an increasing wavelength, the light is reflected to higher angles. This, again, coincides with the grating equation  $p \sin \theta = \frac{m}{n} \lambda$ . For an equal pitch  $p$ , diffraction order  $m$  and refractive index  $n$ , increasing the wavelength scales increasingly with  $\sin \theta$ .

Figure 5.4d shows a cross section of Figure 5.4b, with the relative reflection percentage per degree for  $\lambda = 650$  nm. The blue part of the reflection curve represents the zeroth order reflection and goes out of scale. The real relative reflection for this zeroth order is 1.59% per degree. We observe a broader reflection range for the zeroth order in this measurement than in the simulation. This is due to the fact that the simulation measured the angular distribution in 0.18 degrees while the measurement had a 1 degree precision. The  $\cos \theta$  distribution is presented by the grey dashed line. We show experimentally that the relative reflection per degree follows the cosine law rather well for the angles  $30^\circ - 75^\circ$ . The two high reflection peaks at  $\pm 45^\circ$  correspond to the calculation error that is also present in the simulations. Therefore, we conclude that the experimental results follow the simulation results accurately and hence the fabrication is well executed.

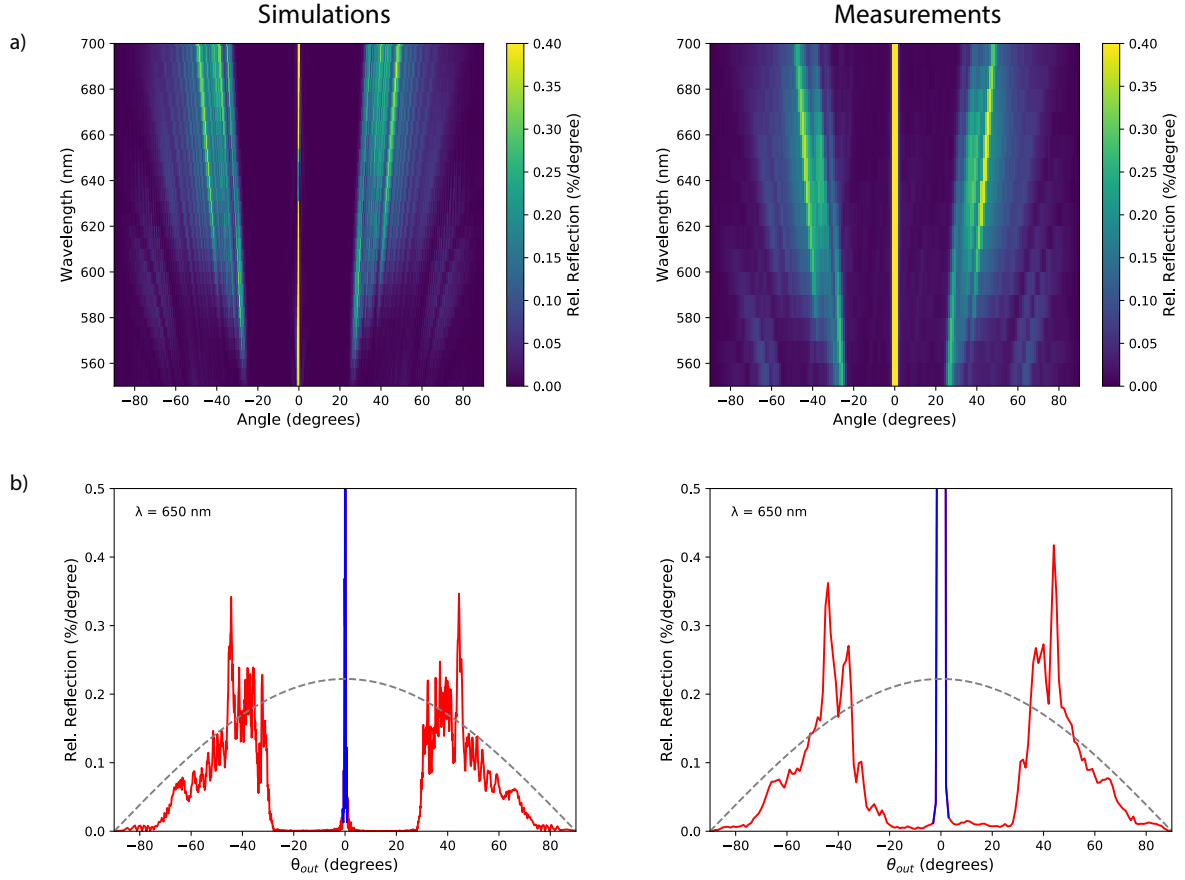


Fig. 5.4: Rotating stage simulations (left) versus measurements (right). a) Relative reflection per degree b) Relative reflection per degree for  $\lambda = 650$  nm.

### 5.3 External quantum efficiency

In the previous section we have experimentally confirmed that, with the current design, it is possible to gain both spectral and angular control over the scattering of light. In order to construct this design in future applications, we demonstrate the possibility of attaching the designed sample on top of a solar cell (Figure 5.5).

Silicon solar cells have a specific external quantum efficiency (EQE). This is ratio of the total number of electrons that can be extracted per incoming photon. An example of a silicon solar cell is given in Figure 5.6 (blue). As silicon is a semiconductor material, it has a specific bandgap that limits the possibility of absorbing photons with energies less than the bandgap. Therefore, the EQE of silicon solar cells is zero below this energy value or above the corresponding wavelength. High energy photons are absorbed close to the surface of the material, leading to high surface recombination and reduced EQE in the low wavelength range.

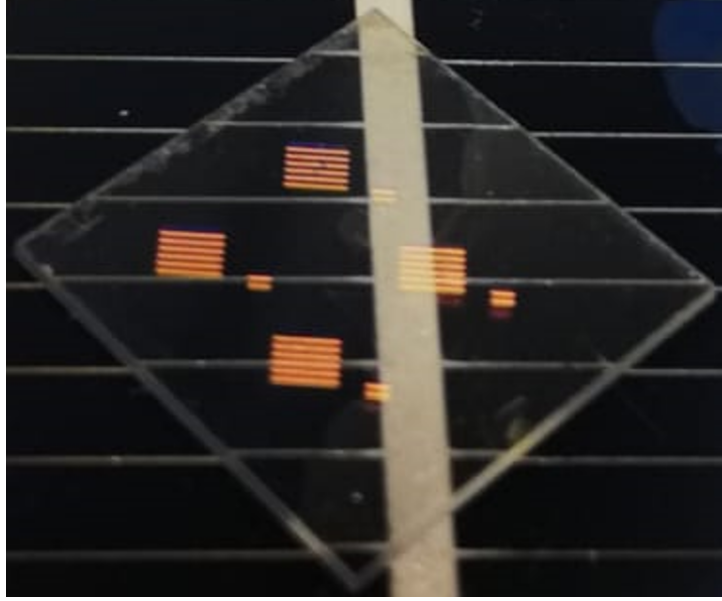


Fig. 5.5: Sample is attached to a bare silicon solar cell using immersion oil. Four colourful patches show four different “supercells” that were each fabricated with a different dose.

In order to analyse the cell’s efficiency, we place the sample containing the nanowires on the solar cell using immersion oil. First, the EQE is measured on the bare sapphire substrate where there are no silicon nanowires (orange). We observe similar effects as for the bare silicon solar cell, with slightly lower EQE over the whole spectrum. The reduction in EQE is a result of the typical reflection of the sapphire, which is around 8% over the visible wavelength range. Next, the EQE is measured on the designed surface (green). It is apparent that the EQE is lower than the EQE of the sapphire, especially below  $\lambda = 800$  nm. Closer analysis show a reduction of the EQE from 600 to 800 nm, which can be accounted for by the enhanced reflection that the cell was designed for. In the lower wavelength range, the EQE is reduced due to the higher absorption in the silicon nanowires. This absorption can be reduced by replacing the silicon with a material with a lower extinction coefficient in this range.

From the external quantum efficiency, it is possible to calculate the short circuit current of the cell. We multiply the EQE data with the electric charge  $q$  and the incoming spectrum of the light  $\Phi(\lambda)$ , given by the number of photons per unit wavelength per unit area per second. Then we integrate this result over all wavelengths to obtain the short circuit current:

$$J_{sc} = q \int_{\lambda_{min}}^{\lambda_{max}} \Phi(\lambda) \cdot EQE(\lambda) \cdot d\lambda \quad (5.1)$$

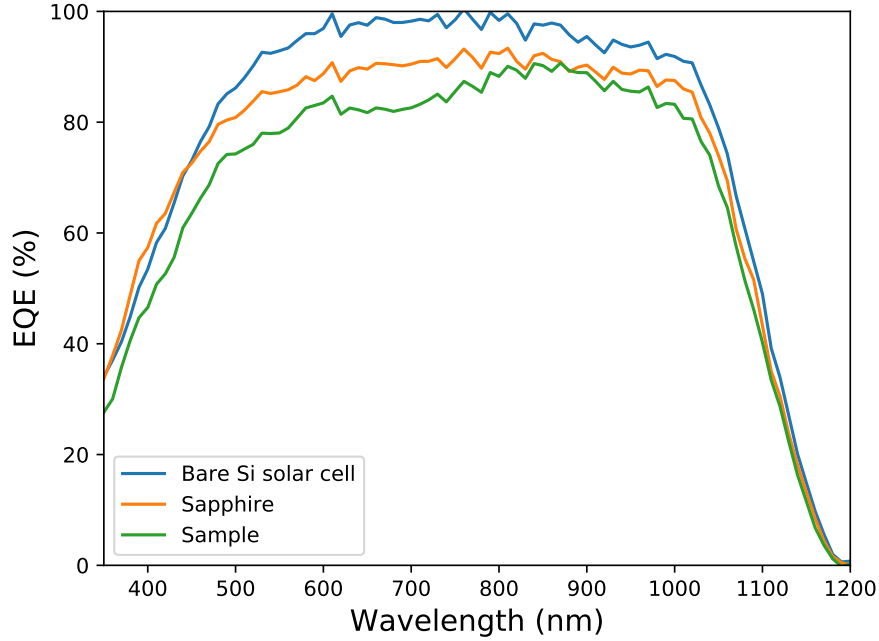


Fig. 5.6: External quantum efficiency (EQE) of a bare silicon solar cell (blue), solar cell + sapphire substrate (orange), solar cell + sapphire + nanowires (green).

For the bare silicon solar cell, we obtain a short circuit current of  $J_{sc} = 38.9 \text{ mA/cm}^2$ , while for the sample we obtain a value of  $J_{sc} = 34.0 \text{ mA/cm}^2$ . Therefore, we conclude that the solar cell including the designed metasurface loses 12% of its efficiency. Current market viable solar panels have an efficiency of around 20%. Should this design be ready to scale up for market production, the efficiency of the coloured solar cell would potentially reach 17.6% efficiency. In relation to various solar panels with extra features such as colour, this design is promising for future research and rooftop applications.

## Chapter 6

---

### Conclusion and outlook

---

In this work we experimentally demonstrate spectral and angular control of light using resonant metagratings viable for future applications in photovoltaics. A transparent layer with nanostructures is designed to reflect a wavelength range around  $\lambda = 650$  nm in order to obtain a 'red' colour in the sample. This layer attached on top of a silicon solar cell for capturing the majority of the transmitted light and generating a current necessary for rooftop photovoltaic applications. Through simulation and fabrication of silicon nanowires on a sapphire substrate, it is possible to tune the spectral response of Mie-like resonances that can be excited. First, the spectral response of Mie-like resonances was simulated using FDTD simulations in Lumerical. Next, the dimensions of a single nanowire were optimized, such that the resonances coincide with the desired wavelength range. Plane wave excitation of the magnetic modes within the particle allow light to be reflected at resonance. As a result, the scattering efficiency is enhanced and the reflection spectrum peaks at the corresponding wavelength(s). These resonant features were demonstrated with reflection measurements using an integrating sphere.

In addition to confirming the spectral control of the reflected light, this work also established angular control of the reflecting surface. Silicon nanowires were placed in multiple gratings, where each grating characterizes the diffraction to the outgoing angle, following the grating equation. The 'supercell' was designed to scatter light to a large range of angles, from  $30^\circ - 75^\circ$ . In this way, the light is scattered only in the first diffraction order, providing full control over the directionality of the reflected light. The zeroth order diffraction is partially interfered destructively by the phase difference with the plane wave sapphire reflection. For the cell to have the same apparent brightness in every angle, the reflection requires the sample to scatter according to the Lambertian cosine law. All

gratings were placed alongside each other, where the number of particles in each grating was optimized to follow this cosine law. This study verified the theoretical simulations of the angular distribution experimentally using a monochromated supercontinuum laser.

Finally, the constructed design was made as an additional layer on top of a silicon solar cell. The transmissive layer demonstrated both the desired angular and spectral reflection distribution while maintaining high transmission through the substrate into the solar cell. External quantum efficiency measurements showed relatively high efficiencies, with short circuit currents only 12% lower than the bare silicon solar cell. The perceived colour of the cell appears a dark orange colour, not too dissimilar of a regular rooftop colour, achieving what was desired for the application. A schematic of the desired reflection mechanism is given in Figure 6.1.

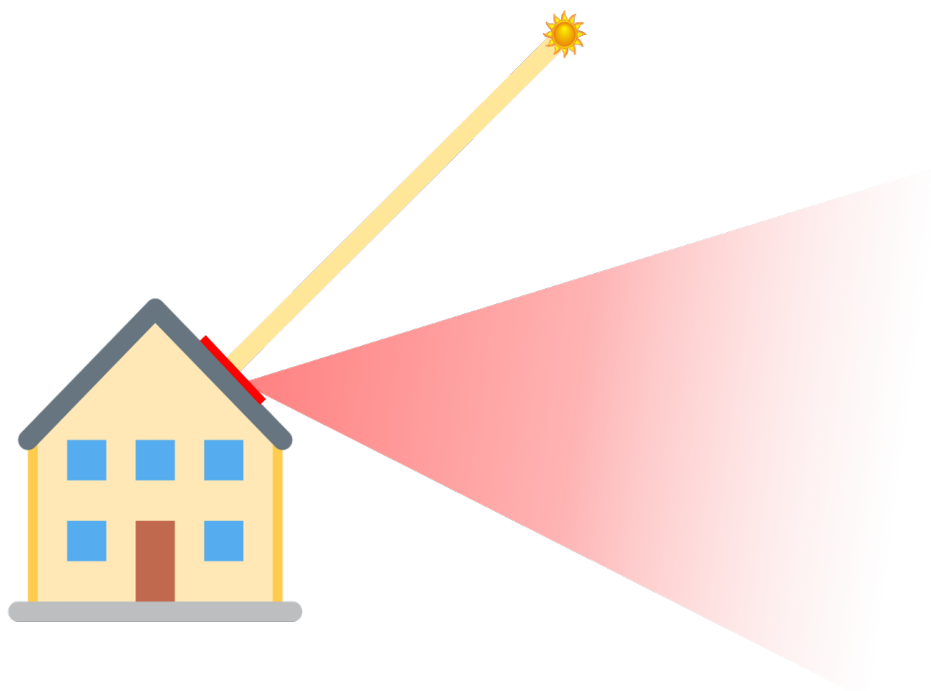


Fig. 6.1: Schematics of a solar panel with broken symmetry scattering red light downwards only.

With the current design, the preliminary results show high potential for future applications. However, there are a number of challenges still to overcome. First of all, the nanowires are placed in two dimensional arrays, causing diffraction in one plane only and is therefore strongly dependent on the polarization of the incoming light. As the direct sunlight is unpolarized, resonances are different from polarized illumination and manipulating the desired reflection is more complicated. For future research, it is interesting to analyse the same design under TM polarization instead of TE. One method to achieve better application properties is to fabricate arrays of three dimensional cylinders.

---

Another method might include combining multiple two dimensional arrays in different orientations to cover more angles of incidence. In some countries, diffuse sunlight governs most of the incoming light. For diffuse light, it might be favorable to fabricate scatterers in subwavelength pitches, possibly encompassing the structures with a reflector such as a Bragg mirror.

Whereas the aim of this study comprised of reflecting light downwards to observers standing below the solar panels on roofs, the symmetry of the current design produces diffraction in the +1 and -1 direction. Consequently, one of the orders reflects downwards as we aspire, while the other order reflects light upwards. This part of the reflection is considered unnecessary, as not many observers view the roof from above and therefore this reflected light is mere additional loss of potential current generation. One approach that could solve this loss is by introducing an asymmetry in the nanostructures. Through placement of two nanowires with dissimilar dimensions next to each other, one could tune the interference of the scattering profiles between the particles such that incoming light will be destructively interfered in one direction while constructively interfering in the other.

Bringing colour to photovoltaics could significantly change the way we perceive self sustainable homes, buildings and other areas in the world. The presented methods are only a few possibilities that could boost future research into providing the photovoltaic applications essential for integrating visually attractive sustainable energy solutions in rural architecture and buildings. The ambition of coloured PV in nanophotonics research lies strongly in designing cost effective and energy efficient applications to ensure the energy transition goals. This study aspires succeeding research to further optimize such metasurfaces for viable photovoltaic applications.



---

# Acknowledgements

---

First of all, I would like to thank my supervisor prof. dr. Albert Polman for giving me the opportunity to write my Master's thesis in his group. In addition to always being there for questions and discussions about the project, he always strived to setting me on the right track. Secondly, I would like to thank dr. Katerina Newell for agreeing to be my second supervisor and for taking the time to read the thesis.

A big thank you to my daily supervisor Verena, who has pushed me into theory, simulation and the cleanroom directly from the start, and amazingly had the time to supervise me next to her amazing journey into becoming the perfect mother of a beautiful daughter, Clara. And many thanks to my second supervisor Andrea, who was my personal manager in teaching me how to dig deep and understand complicated theories and showing me how many mistakes it takes to become a pro in nanofabbing. And of course a big thanks to the daily moral support and great chats from the Photonic Materials group.

These 10 months have been challenging, interesting, educational, fabrication and powerful with many ups and downs. Working in this group at AMOLF has truly shown me what research is and what it means to society. I am very glad to have had the opportunity to dig deep and create a full storyline of the coloured solar panel. Even though I will not continue in research now, I will always look back on this project, the people and the atmosphere at AMOLF with a smile on my face.



# Appendix A

---

## Appendix

---

### A.1 Material Characterization

A considerable part of this study was dedicated to determining the material to work with. Initially, simulations and fabrication were performed using evaporated silicon on quartz substrates. However, it is difficult to obtain monocrystalline silicon by evaporation. Therefore, in the final design, crystalline silicon on sapphire substrates were bought and used in the fabrication. This section is an additional part demonstrating possible methods to crystallize silicon.

The silicon was evaporated using electron-beam physical vapor deposition (EBPVD) at 500°C. During evaporation at high temperatures, the silicon crystallizes according to the evaporation rate and temperature. Additional analysis was done in determining the merit of crystallization of the silicon. After EBPVD at 500°C, the sample was annealed using Rapid Thermal Annealing (RTA) at temperatures from 800°C to 1100°C. It was assumed that the silicon crystallizes more at higher temperatures. In order to evaluate the grade of crystallization, there were two factors to be analyzed: optical constants and X-ray Diffraction (XRD).

#### A.1.1 Ellipsometry for determining optical constants

Ellipsometry is a commonly used technique for determining the refractive index of the material [41]. The optical constants of ellipsometry analysis of annealed and non annealed silicon (all evaporated at 500°C) are given in Figure A.1. In order to compare the type of silicon, Figure A.2 shows the optical constants for amorphous, polycrystalline silicon

and monocrystalline silicon. The main point of the crystallization is to obtain a material with the least amount of absorption, such that the reflection and transmission of the final cell are optimal. We observe in the optical constants data that the refractive index  $n$  decreases slightly with higher annealing temperatures. This is a result of the silicon crystallizing from amorphous (not annealed) towards polycrystalline silicon (annealed). Furthermore, the imaginary part of the refractive index  $\kappa$ , or the extinction coefficient, decreases significantly in the shorter wavelength range. At  $\lambda = 400$  nm,  $\kappa$  drops below 0.8, which is in accordance of the  $\kappa$  in polycrystalline silicon. We therefore assume that the high temperature annealed and evaporated silicon is polycrystalline silicon.

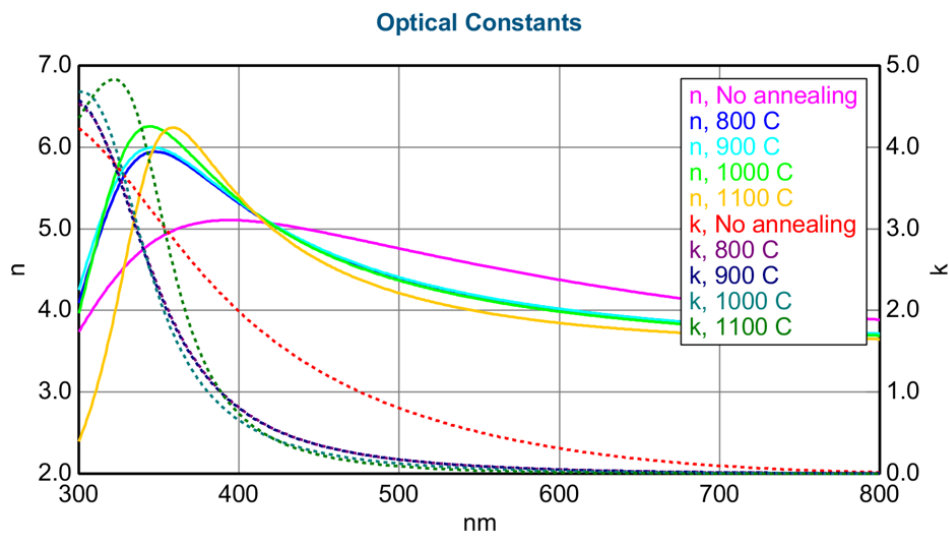


Fig. A.1: Optical constants, both  $n$  and  $\kappa$ , of evaporated and annealed silicon. All samples evaporated at  $500^{\circ}\text{C}$ , one without additional annealing and four samples with high temperature annealing  $800^{\circ}\text{C}$  to  $1100^{\circ}\text{C}$ .

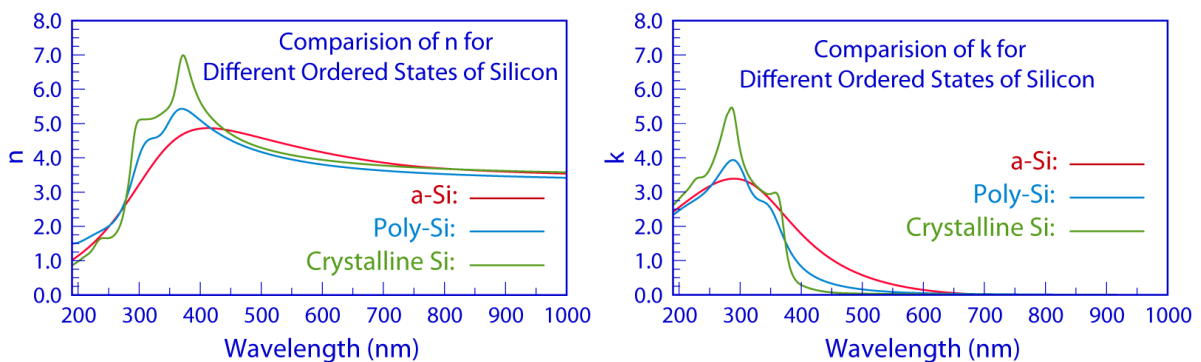


Fig. A.2: Optical constants of amorphous silicon (a-Si), polycrystalline silicon (Poly-Si) and monocrystalline silicon (Crystalline Si). a) Refractive index  $n$  as a function of wavelength b) Extinction coefficient  $\kappa$  as a function of wavelength. Figures taken from [42].

### A.1.2 X-ray Diffraction to determine grain size of crystalline silicon

In order to prove this more extensively, X-ray Diffraction was performed (Figure A.3). The crystalline structure of the material causes a beam of incident X-rays to diffract into many specific directions. The intensity measured in each direction gives information about the crystalline structure and grain size of the material. For the silicon that was not annealed, there is barely any crystalline structure in the material, resulting in a broad and highly fluctuating angular spectrum (Fig A.3a). The big peak around  $2\theta = 20$  accounts for the reflection of the glass substrate. Therefore, the unannealed silicon is highly amorphous. For monocrystalline silicon (fully single crystalline silicon sample, Fig. A.3b), there is only one crystal size in the whole material. This results in all the X-ray beams being diffracted at one angle (in this case  $2\theta = 70$ ). For polycrystalline silicon, the material has multiple crystalline structures and multiple grain sizes, resulting in multiple diffraction peaks. Figure A.3c shows XRD on the silicon sample that was annealed to  $1000^\circ\text{C}$ . A clear peak at  $2\theta = 43$  arises and is displayed zoomed in Figure A.3d.

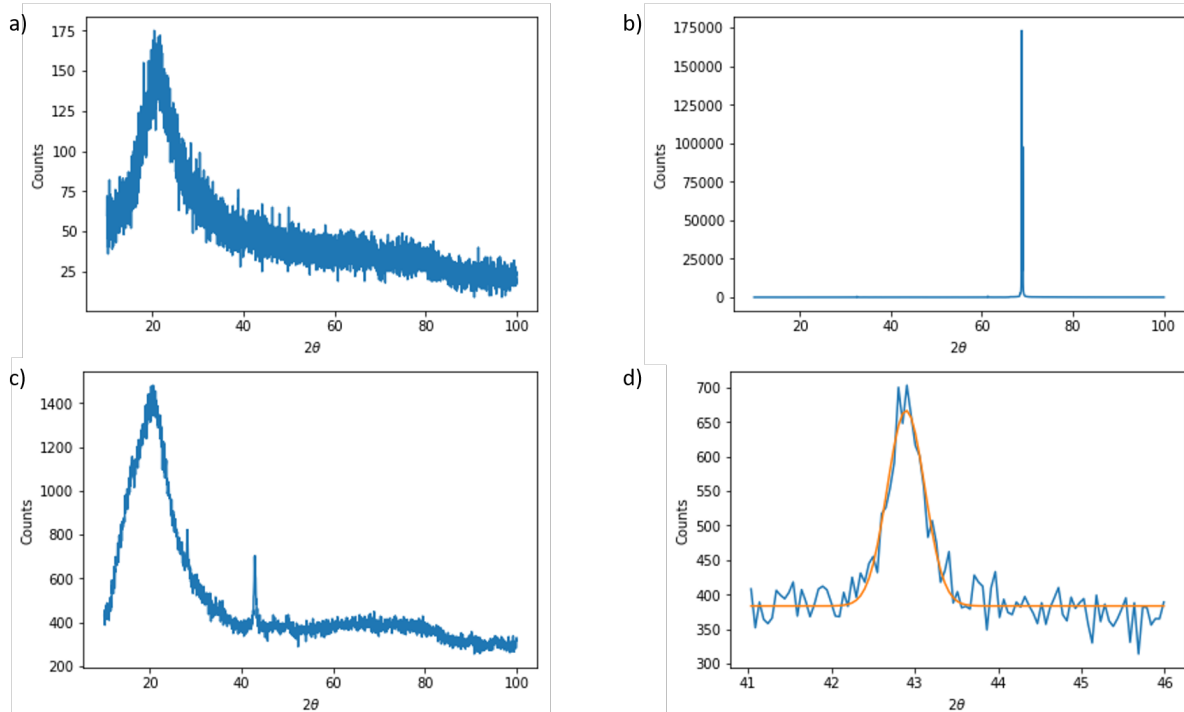


Fig. A.3: X-ray diffraction shows number of counts in each direction  $2\theta$  for a) Amorphous silicon b) Monocrystalline silicon c) Annealed silicon at  $1000^\circ\text{C}$  d) Zoomed in part of Figure c, showing the fit of the peak.

With a fitted Gaussian curve (orange), we can determine the grain size of the material with the Scherrer equation:

$$\tau = \frac{k\lambda}{\beta \cos \theta} \quad (\text{A.1})$$

where  $\tau$  is the grain size to be calculated,  $k$  is the shape factor,  $\lambda$  is the X-ray wavelength,  $\beta$  is the full width half maximum (FWHM) of the peak and  $\theta$  is the Bragg diffraction angle. The peak in Fig. A.3d is at  $2\theta = 42.3^\circ$ . From the Gaussian fit we obtain a FWHM of  $\beta = 0.000836$ . The X-ray wavelength is  $\lambda = 1.54 \text{ \AA}$  and the general shape factor is  $k = 0.9$  for spherical grains (assuming the grains are almost spherical). Then, by filling in the Scherrer equation, we obtain a grain size of  $\tau = 22.6 \text{ nm}$ . The peak at  $2\theta = 42.3^\circ$  is the most enhanced peak. There are other peaks in the spectrum of Fig. A.3c, accounting for other grain sizes, but most grains are of the size  $\tau = 22.6 \text{ nm}$ . Consequently, the material is characterized as polycrystalline silicon, due to the multiple small grain sizes. For the continuation of the study, this polycrystalline silicon was not used further and only characterized here.

---

# Bibliography

---

- [1] Mehreen Gul, Yash Kotak, and Tariq Muneer. Review on recent trend of solar photovoltaic technology. *Energy Exploration & Exploitation*, 34(4):485–526, 2016.
- [2] Patrick Heinstein, Christophe Ballif, and Laure-Emmanuelle Perret-Aebi. Building integrated photovoltaics (bipv): review, potentials, barriers and myths. *Green*, 3(2):125–156, 2013.
- [3] A Schueler, C Roecker, J-L Scartezzini, J Boudaden, IR Videnovic, RS-C Ho, and P Oelhafen. On the feasibility of colored glazed thermal solar collectors based on thin film interference filters. *Solar Energy Materials and Solar Cells*, 84(1-4):241–254, 2004.
- [4] A Schüler, J Boudaden, P Oelhafen, E De Chambrier, C Roecker, and J-L Scartezzini. Thin film multilayer design types for colored glazed thermal solar collectors. *Solar Energy Materials and Solar Cells*, 89(2-3):219–231, 2005.
- [5] Minghua Li, Libin Zeng, Yifeng Chen, Lin Zhuang, Xuemeng Wang, and Hui Shen. Realization of colored multicrystalline silicon solar cells with  $\text{SiO}_2/\text{SiNx}$ : H double layer antireflection coatings. *International Journal of Photoenergy*, 2013, 2013.
- [6] S Péliisset, M Joly, V Chapuis, A Schüler, S Mertin, Hody-Le Caër, C Ballif, L-E Perret-Aebi, et al. Efficiency of silicon thin-film photovoltaic modules with a front coloured glass. In *Proceeding of the CISBAT International Conference 2011*, number CONF, pages 37–42. EPFL, 2011.
- [7] J Van de Groep and A Polman. Designing dielectric resonators on substrates: Combining magnetic and electric resonances. *Optics express*, 21(22):26285–26302, 2013.
- [8] Ramón Paniagua-Domínguez, Ye Feng Yu, Andrey E Miroshnichenko, Leonid A Krivitsky, Yuan Hsing Fu, Vytautas Valuckas, Leonard Gonzaga, Yeow Teck Toh,

- Anthony Yew Seng Kay, Boris Luk'yanchuk, et al. Generalized brewster effect in dielectric metasurfaces. *Nature communications*, 7:10362, 2016.
- [9] Eun-Hyoung Cho, Hae-Sung Kim, Byoung-Ho Cheong, Prudnikov Oleg, Wenxu Xi-anya, Jin-Seung Sohn, Dong-Joon Ma, Hwan-Young Choi, No-Cheol Park, and Young-Pil Park. Two-dimensional photonic crystal color filter development. *Optics express*, 17(10):8621–8629, 2009.
- [10] Linyou Cao, Pengyu Fan, Edward S Barnard, Ana M Brown, and Mark L Brongersma. Tuning the color of silicon nanostructures. *Nano letters*, 10(7):2649–2654, 2010.
- [11] Yoshiaki Kanamori, Toshikazu Ozaki, and Kazuhiro Hane. Reflection color filters of the three primary colors with wide viewing angles using common-thickness silicon subwavelength gratings. *Optics express*, 22(21):25663–25672, 2014.
- [12] Julien Proust, Frédéric Bedu, Bruno Gallas, Igor Ozerov, and Nicolas Bonod. All-dielectric colored metasurfaces with silicon mie resonators. *Acs Nano*, 10(8):7761–7767, 2016.
- [13] Shang Sun, Zhenxing Zhou, Chen Zhang, Yisheng Gao, Zonghui Duan, Shumin Xiao, and Qinghai Song. All-dielectric full-color printing with tio2 metasurfaces. *ACS nano*, 11(5):4445–4452, 2017.
- [14] Verena Neder, Stefan L Luxembourg, and Albert Polman. Efficient colored silicon solar modules using integrated resonant dielectric nanoscatterers. *Applied Physics Letters*, 111(7):073902, 2017.
- [15] Verena Neder, Younes Ra'di, Andrea Alù, and Albert Polman. Combined metagratings for efficient broad-angle scattering metasurface. *ACS Photonics*, 2019.
- [16] Lukas Novotny and Bert Hecht. *Principles of nano-optics*. Cambridge university press, 2012.
- [17] Alexandra Boltasseva and Harry A Atwater. Low-loss plasmonic metamaterials. *Science*, 331(6015):290–291, 2011.
- [18] Arseniy I Kuznetsov, Andrey E Miroshnichenko, Mark L Brongersma, Yuri S Kivshar, and Boris Luk'yanchuk. Optically resonant dielectric nanostructures. *Science*, 354(6314):aag2472, 2016.

- [19] Andrey B Evlyukhin, Carsten Reinhardt, Andreas Seidel, Boris S Luk'yanchuk, and Boris N Chichkov. Optical response features of si-nanoparticle arrays. *Physical Review B*, 82(4):045404, 2010.
- [20] Aitzol Garcia-Etxarri, R Gómez-Medina, Luis S Froufe-Perez, Cefe Lopez, L Chantada, Frank Scheffold, J Aizpurua, M Nieto-Vesperinas, and Juan José Sáenz. Strong magnetic response of submicron silicon particles in the infrared. *Optics express*, 19(6):4815–4826, 2011.
- [21] Arseniy I Kuznetsov, Andrey E Miroshnichenko, Yuan Hsing Fu, JingBo Zhang, and Boris Luk'Yanchuk. Magnetic light. *Scientific reports*, 2:492, 2012.
- [22] Yan Zhang, Manuel Nieto-Vesperinas, and Juan José Sáenz. Dielectric spheres with maximum forward scattering and zero backscattering: a search for their material composition. *Journal of Optics*, 17(10):105612, 2015.
- [23] Boris S Luk'yanchuk, Nikolai V Voshchinnikov, Ramón Paniagua-Domínguez, and Arseniy I Kuznetsov. Optimum forward light scattering by spherical and spheroidal dielectric nanoparticles with high refractive index. *ACS Photonics*, 2(7):993–999, 2015.
- [24] Andrey B Evlyukhin, Carsten Reinhardt, and Boris N Chichkov. Multipole light scattering by nonspherical nanoparticles in the discrete dipole approximation. *Physical Review B*, 84(23):235429, 2011.
- [25] Isabelle Staude, Andrey E Miroshnichenko, Manuel Decker, Nche T Fofang, Sheng Liu, Edward Gonzales, Jason Dominguez, Ting Shan Luk, Dragomir N Neshev, Igal Brener, et al. Tailoring directional scattering through magnetic and electric resonances in subwavelength silicon nanodisks. *ACS nano*, 7(9):7824–7832, 2013.
- [26] Yuan Hsing Fu, Arseniy I Kuznetsov, Andrey E Miroshnichenko, Ye Feng Yu, and Boris Luk'yanchuk. Directional visible light scattering by silicon nanoparticles. *Nature communications*, 4:1527, 2013.
- [27] Andrey B Evlyukhin, Sergey M Novikov, Urs Zywiets, Rene Lynge Eriksen, Carsten Reinhardt, Sergey I Bozhevolnyi, and Boris N Chichkov. Demonstration of magnetic dipole resonances of dielectric nanospheres in the visible region. *Nano letters*, 12(7):3749–3755, 2012.
- [28] Craig F Bohren and Donald R Huffman. *Absorption and scattering of light by small particles*. John Wiley & Sons, 2008.

- [29] Christopher L Holloway, Edward F Kuester, Joshua A Gordon, John O'Hara, Jim Booth, and David R Smith. An overview of the theory and applications of metasurfaces: The two-dimensional equivalents of metamaterials. *IEEE Antennas and Propagation Magazine*, 54(2):10–35, 2012.
- [30] Carl Pfeiffer and Anthony Grbic. Metamaterial huygens' surfaces: tailoring wave fronts with reflectionless sheets. *Physical review letters*, 110(19):197401, 2013.
- [31] Younes Ra'di, Dimitrios L Sounas, and Andrea Alu. Metagratings: beyond the limits of graded metasurfaces for wave front control. *Physical review letters*, 119(6):067404, 2017.
- [32] Yang Zhao, Xing-Xiang Liu, and Andrea Alù. Recent advances on optical metasurfaces. *Journal of Optics*, 16(12):123001, 2014.
- [33] Nanfang Yu and Federico Capasso. Flat optics with designer metasurfaces. *Nature materials*, 13(2):139, 2014.
- [34] SA Tretyakov. Metasurfaces for general transformations of electromagnetic fields. *Philosophical Transactions of the Royal Society A: Mathematical, Physical and Engineering Sciences*, 373(2049):20140362, 2015.
- [35] Nanfang Yu, Patrice Genevet, Mikhail A Kats, Francesco Aieta, Jean-Philippe Tetienne, Federico Capasso, and Zeno Gaburro. Light propagation with phase discontinuities: generalized laws of reflection and refraction. *science*, 334(6054):333–337, 2011.
- [36] Stanislav B Glybovski, Sergei A Tretyakov, Pavel A Belov, Yuri S Kivshar, and Constantin R Simovski. Metasurfaces: From microwaves to visible. *Physics reports*, 634:1–72, 2016.
- [37] Shulin Sun, Kuang-Yu Yang, Chih-Ming Wang, Ta-Ko Juan, Wei Ting Chen, Chun Yen Liao, Qiong He, Shiyi Xiao, Wen-Ting Kung, Guang-Yu Guo, et al. High-efficiency broadband anomalous reflection by gradient meta-surfaces. *Nano letters*, 12(12):6223–6229, 2012.
- [38] Johann Heinrich Lambert. *Pyrometrie*. bey Haude und Spener, 1779.
- [39] Edward D Palik. *Handbook of optical constants of solids*, volume 3. Academic press, 1998.

- [40] Gunter Wyszecki and Walter Stanley Stiles. *Color science*, volume 8. Wiley New York, 1982.
- [41] Harland Tompkins and Eugene A Irene. *Handbook of ellipsometry*. William Andrew, 2005.
- [42] Wikipedia contributors. Refractive index and extinction coefficient of thin film materials — Wikipedia, the free encyclopedia, 2019. [Online; accessed 22-July-2019].

## Bibliography

---

I hereby declare that the work presented here was formulated by myself and that no sources or tools other than those cited were used.

Amsterdam, .....  
July 22, 2019  
date

.....  
  
signature